

The rise of fully turbulent flow

Dwight Barkley¹, Baofang Song^{2,3}, Vasudevan Mukund², Grégoire Lemoult²,
Marc Avila⁴, and Björn Hof^{2*}

6 June, 2015

¹ Mathematics Institute, University of Warwick, Coventry, CV4 7AL, United Kingdom

² Institute of Science and Technology Austria, 3400 Klosterneuburg, Austria

³ Institute of Multiscale Simulation, Friedrich-Alexander-Universität, Erlangen, Germany

⁴ Institute of Fluid Mechanics, Friedrich-Alexander-Universität, Erlangen, Germany

* email: bhof@ist.ac.at

This manuscript is the original submission to Nature. The final (published) version can be
accessed at <http://www.nature.com/nature/journal/v526/n7574/full/nature15701.html>

Over a century of research into the origin of turbulence in wallbounded shear flows has resulted in a puzzling picture in which turbulence appears in a variety of different states competing with laminar background flow.¹⁻⁶ At slightly higher speeds the situation changes distinctly and the entire flow is turbulent. Neither the origin of the different states encountered during transition, nor their front dynamics, let alone the transformation to full turbulence could be explained to date. Combining experiments, theory and computer simulations here we uncover the bifurcation scenario organising the route to fully turbulent pipe flow and explain the front dynamics of the different states encountered in the process. Key to resolving this problem is the interpretation of the flow as a bistable system with nonlinear propagation (advection) of turbulent fronts. These findings bridge the gap between our understanding of the onset of turbulence⁷ and fully turbulent flows.^{8,9}

The sudden appearance of localised turbulent patches in an otherwise quiescent flow was first observed by Osborne Reynolds for pipe flow¹ and has since been found to be the starting point of turbulence in most shear flows.^{2,4,10-15} Curiously, in this regime it is impossible to maintain turbulence over extended regions as it automatically^{16,17} reduces to patches of characteristic size, called puffs in pipe flow (see Fig. 1a). Puffs can decay, or else split and thereby multiply. Once the Reynolds number $R > 2040$ the splitting process outweighs decay, resulting in sustained disordered motion.⁷ Although sustained, turbulence at these low R only consists of puffs surrounded by laminar flow (Fig. 1a) and cannot form larger clusters.^{17,18}

At larger flow rates, the situation is fundamentally different: once triggered, turbulence aggressively expands and eliminates all laminar motion (Fig. 1b). Fully turbulent flow is now the natural state of the system and only then do wallbounded shear flows have characteristic mean properties such as the Blasius or Prandtl-von Karman friction laws.⁹ This rise of fully turbulent flow has remained unexplained despite the fact that this transformation occurs in virtually all shear flows and generally dominates the dynamics at sufficiently large Reynolds numbers.

A classical diagnostic for the formation of turbulence^{2-5,19,20} is the propagation speed of the

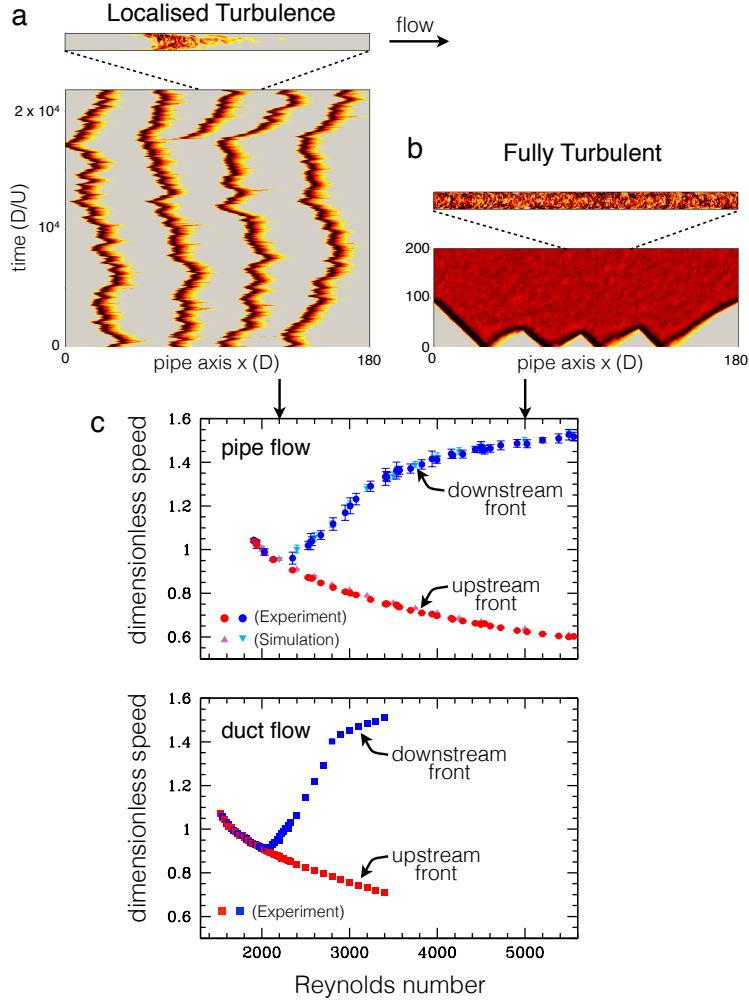


Figure 1: **Localised and fully turbulent flow.** **a**, **b**, numerical simulations of pipe flow illustrate the distinction between **(a)** localised turbulence, at $R = 2200$ and **(b)** fully turbulent flow, at $R = 5000$. In each case, the flow is initially seeded with localised turbulent patches and the subsequent evolution is visualised via space-time plots in a reference frame co-moving with structures. Colours indicate the value of $\sqrt{u_r^2 + u_\theta^2}$. Further highlighting the distinction between cases, shown at the top are cross sections of instantaneous flow within the pipe. A 35D section is shown with the vertical direction stretched by a factor of 2. While the protocol used here is seeding the flow with localised patches of turbulence, the fundamental distinction between localised and fully turbulent flow is independent of how turbulence is triggered.¹⁶ **c**, Speeds of turbulent-laminar fronts as a function of Reynolds number for pipe flow and duct flow. A speed difference between the upstream and downstream fronts corresponds to expanding turbulence, and asymptotically, to a fully turbulent flow.

upstream and downstream fronts for a turbulent patch. We have carried out such measurements for pipe and square duct flow (Fig. 1c), focusing on the regime where turbulence first begins to expand. In both experiments, fluid enters the conduit through a smoothly contracting inlet, ensuring that without external perturbations flows are laminar over the entire Reynolds number regime investigated. Turbulence is triggered $120D$ from the inlet by a short-duration, localised perturbation. A pressure sensor at the outlet determines the subsequent arrival of first the downstream and then the upstream turbulent-laminar front. Speeds are averaged over many realisations for each R , giving a total travel distance of typically $5 \times 10^4 D$. As an independent verification, speeds in pipe flow were determined through extensive direct numerical simulations in pipes of length $180D$, with averaging over large ensembles.

In both flows, initially the speeds of the downstream fronts are indistinguishable from the upstream ones, signalling localised turbulence. For $R \gtrsim 2250$ in pipe flow and $R \gtrsim 2030$ in duct flow, the downstream speed increases with R , marking the point where turbulence begins to aggressively invade the surrounding fluid. With further increases in R the downstream front speeds exhibits complex changes of curvature as a function of R . Surprisingly, the spreading of turbulence shows neither a square-root scaling nor an exponent associated with a percolation type processes, as proposed in earlier studies.^{4,21} The speed of the downstream spreading has a far more complex behaviour than these theories imply.

In a theoretical approach,^{22–24} puffs in pipe flow were categorised as localised excitations analogous to action potentials in axons and from this numerous features of puff turbulence were captured. However, in that model the transition leading to an expanding state is first-order (discontinuous), not reflecting the observed continuous behaviour at the onset of fully turbulent flow (Fig. 1c). This model did not, however, include nonlinear advection, a feature intrinsic to fluid dynamics. We have devised an extended model incorporating advective nonlinearity that fully captures the sequence encountered in the route to fully turbulent flow. The model is

$$q_t + (u - \zeta)q_x = f(q, u) + Dq_{xx}, \quad u_t + uu_x = \epsilon g(q, u) \quad (1)$$

where,

$$f(q, u) = q(r + u - 2 - (r + 0.1)(q - 1)^2), \quad g(q, u) = 2 - u + 2q(1 - u) \quad (2)$$

Subscripts denote derivatives. Variables q and u depend only on the streamwise coordinate x and time t . q represents the turbulence level while u represents the centreline velocity and plays two important roles. It accounts for nonlinear advection in the streamwise direction and it models the state of the shear profile: $u = 2$ for parabolic flow and $u < 2$ for plug flow. The functions $f(q, u)$ and $g(q, u)$ capture the known interplay between turbulence (the excited state), and the shear profile.^{3,22} Parameter r plays the role of Reynolds number, ζ accounts for the fact that turbulence is advected more slowly than the centreline velocity, D controls the coupling strength of the turbulent field, and ϵ sets the timescale ratio between fast excitation of q and slow recovery of u following relaminarisation. The fast scale of q and cubic nonlinearity in $f(q, u)$ are motivated by known upper- and lower-branch exact coherent structures in shear flows.²⁵⁻²⁷ (See SI for details.)

To elucidate the core of the transition from localised to expanding excitations, and to identify the different states occurring in the process, we carry out a standard asymptotic analysis^{28,29} in the limit of sharp fronts ($\epsilon \rightarrow 0$). Three distinct turbulent structures are predicted: a localised state (Fig. 2a), an asymmetric expanding state (Fig. 2b), and a symmetric expanding one (Fig. 2c). The essence of each state is clearly seen in the local phase plane (Fig. 2d,e,f). Equilibrium points are located at the intersections of the q and u nullclines (curves where derivatives of u and q are zero). For low values of r (Fig. 2d) the only equilibrium is ($u = 2, q = 0$), corresponding to parabolic laminar flow. Nevertheless, the system can be excited locally; when perturbed the state jumps to the upper branch q^+ . This forms the upstream laminar-to-turbulent front. On the upper branch, $\dot{u} < 0$ and u decreases to a point where turbulence is not maintained and the system jumps back to $q = 0$, forming the downstream front. The downstream front simply follows the upstream one by a fixed distance, thus creating a localised excitation: a puff in pipe flow analogous to an action potential in excitable media.^{24,28,29}

For larger values of r , a second stable equilibrium appears (uppermost intersection of the

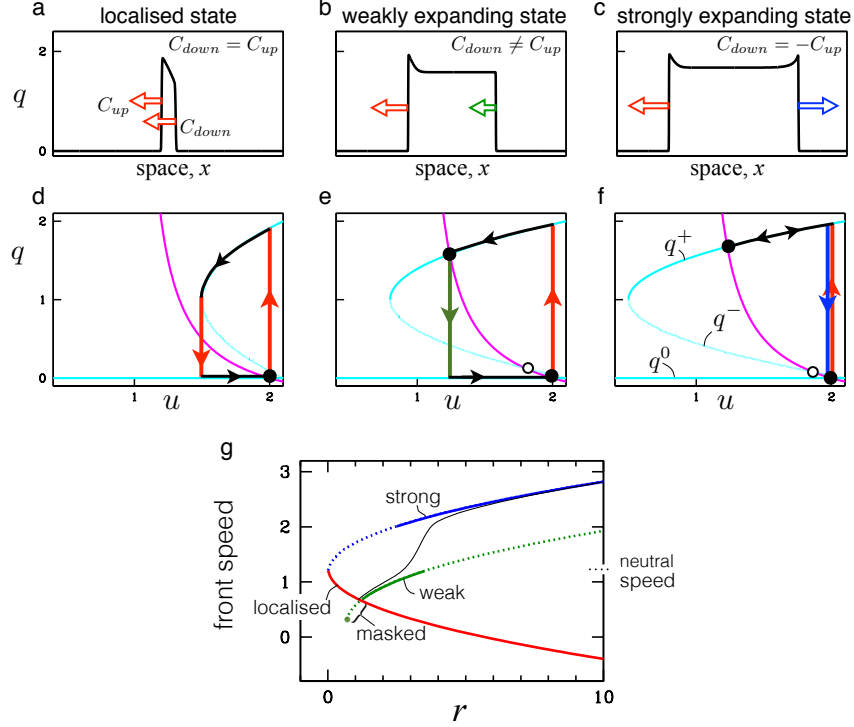


Figure 2: **Model predictions in the asymptotic limit of sharp fronts.** **a-c**, Three distinct types of predicted states. C_{up} and C_{down} are the upstream and downstream front speeds. **d-f**, corresponding states seen in the local phase plane with arrows indicating increasing space coordinate x , (not time). The q -nullcline, (cyan, given by $f(q, u) = 0$, for clarity only labelled in **f**), has three branches since f is cubic in q : stable laminar $q^0 = 0$ and upper q^+ branches and an unstable branch q^- separating the two. The u -nullcline (magenta, given by $g(q, u) = 0$), describes the decrease in the centreline velocity in the presence of turbulence and its recovery in the absence of turbulence. Fronts are jumps between stable branches of the q nullcline. In all cases, the upstream front is a transition from laminar flow (the equilibrium at $u = 2, q = 0$) to the upper branch. The cases are distinguished by the downstream front. In **a, d** the system is excitable and the downstream transition, from q^+ to q^0 , is unrestricted by the upper branch and the speed will be selected to match the upstream front $C_{down} = C_{up}$, thus giving localised turbulence. In **b, e** the system has become bistable with the formation of an upper branch steady state. Evolution on the upper branch is restricted by this state so the downstream front speed may no longer be able match the upstream front speed: $C_{down} \neq C_{up}$ in general. The turbulent patch expands. In **c, f** the upstream and downstream fronts have the same character but move in opposite directions $C_{down} = -C_{up}$ in a reference frame moving at the neutral speed. We refer to the downstream fronts in **b, e** as weak fronts and those in **c, f** as strong fronts. **g**, Front speeds as a function of model Reynolds number r . The nominal critical point for the onset of fully turbulent flow is masked. The neutral speed is the speed about which the upstream and strong downstream fronts speeds are symmetric. At finite ϵ the transition from weak to strong scaling is continuous (black curve).

nullclines in Fig. 2e,f), and the system is now bistable. Here fully turbulent flow begins to arise. The downstream front lags the upstream front giving rise to a growing turbulent region between. Initially the downstream front is tame and expansion is modest. The drop from q^+ to $q = 0$ occurs directly from the upper equilibrium (Fig. 2d,e). We refer to this as the *weak front state*. For larger r the weak front becomes unstable giving rise to the final state, a much more rapidly expanding *strong front state* (Fig. 2c,f). The strong downstream front is the mirror image of the upstream front with an overshoot of q in space and a drop from q^+ to $q = 0$ at $u = 2$ in the phase plane. The downstream speed is opposite the upstream speed with respect to what we term the *neutral speed*.

Before comparing the model to the experimental data, we discuss features of the front-speed scaling that are intrinsic to this model. Figure 2g shows front speeds of the three states. Starting at low r , excitations are strictly localised and their speed monotonically decreases with r (red curve). Expanding turbulence is first encountered when this curve is intersected by the weak-front curve (green). Interestingly, the turbulent state (upper fixed point) bifurcates at lower r , but initially the downstream speed is smaller than the upstream one resulting in a contraction back to a localised excitation. Thus onset of bistability and the expansion do not coincide, masking the transition and resulting in a non-standard front speed scaling. (In contrast to the case without nonlinear advection shown in Fig. S1a). The strong front (blue) is stable at slightly higher r (solid portion of curve) and is perfectly symmetric to the downstream front (red) about the neutral speed. In the asymptotic limit ($\epsilon \rightarrow 0$), weak and strong fronts co-exist over a range of r , but for finite ϵ the front speed continuously varies from a weak to increasingly strong front (solid black curve). During this adjustment the front speed exhibits two curvature changes. This, together with the eventual approach to the upper branch of the parabola are distinct signatures of the scenario described by this model.

Using the theoretical model as a guide, we collapse the measured front speeds from pipe and duct flow and compare them directly with theory (Fig. 3a). Initially, at lower values of R , turbulent excitations are localised (as illustrated for duct flow in Fig. 3b and pipe flow in Fig. 3e) and the front speed data from both flows collapse and agree very well with the parabolic scaling

predicted by the model asymptotics (solid red curve). At $R \approx 2250$ in pipe flow and $R \approx 2030$ in duct flow, expansion begins with the formation of the weak downstream front (illustrated for duct and pipe flow in Figs. 3c and 3f respectively). While upstream fronts of both data sets continue following the simple asymptotic form, the weak downstream fronts do not collapse to a single scaling. Nevertheless, with appropriate choices of parameters ζ and ϵ , the model precisely captures the two curvature changes (solid black curves) encountered as each flow continuously adjusts from the weak front (green dashed) to ultimately the strong front (blue dashed), corresponding to the emergence of the final strong front state (Figs. 3d and 3g). As the downstream front approaches the scaling given by the strong-front asymptotics, its speed indeed forms a parabola with the upstream front speed, a feature systematically overlooked in previous studies.

There are two features of pipe and duct turbulence that the model does not capture. Both originate from stochastic fluctuations within turbulence and are most prevalent when turbulence first begins to expand (Fig. 3c, 3f). Fronts fluctuate, especially the downstream front, and it is common for the system to exhibit sometimes a strong and sometimes a weak downstream front. The bifurcation scenario predicted by the model is only recovered in average quantities. Likewise, turbulence in this regime is not always uniform, but commonly contains intermittent laminar pockets.^{16,30}

Nevertheless, the simplicity of the model permits investigation of new phenomena associated with fully turbulent flow. In the model the creation of extended turbulent regions hinges on the upper intersection of the q and u nullclines. The variable u corresponds to profile shape in pipe flow and this can be manipulated. As suggested by the model, deformation of the profile can indeed eliminate the upper turbulent fixed point and hence relaminarise turbulent flow (demonstrated in the SI), offering a very simple and robust way to control turbulence and to reduce frictional drag.

While in recent years much progress has been made in our understanding of how turbulence in wallbounded flows is formed from unstable invariant solutions^{25–27} at moderate R , little to no progress has been made in connecting this transitional regime to studies of high- R turbulence.

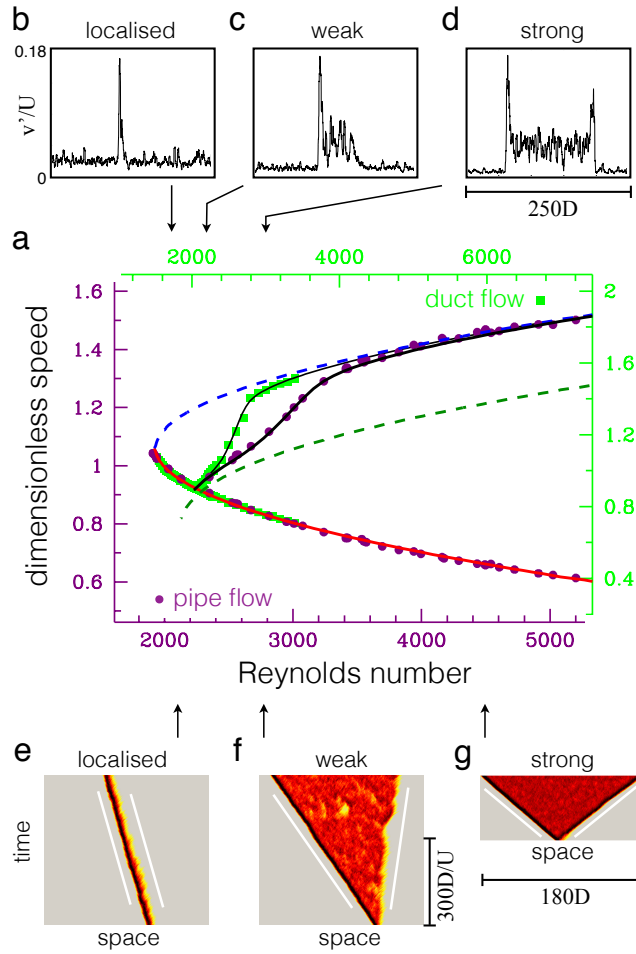


Figure 3: **The rise of fully turbulent flow.** **a**, front speeds as a function of Reynolds number for pipe and duct flow. Points are experimental results from Fig. 1c. Red, blue, and dark green curves are front speeds in the asymptotic limit of sharp fronts (as in Fig. 2g). The only model parameter used for these curves is $D = 0.13$. Black curves are the downstream front speed at finite front width ($\epsilon = 0.2$, $\zeta = 0.79$ for pipe flow and $\epsilon = 0.11$, $\zeta = 0.56$ for duct flow). The distinct weak and strong asymptotic branches (dashed) form the skeleton for the formation of fully turbulent flow, while at finite front width the model captures the complex behaviour of front speeds as a smooth switching between the asymptotic branches. **b-d**, crossstream velocity fluctuations for the three front states in a square duct: localised puff ($R = 1700$), expanding turbulence with a weak downstream front ($R = 2300$) and the strong front state ($R = 3000$), exhibiting the characteristic energy overshoot at the downstream edge.^{5,20} **e-g**, Space-time plots from simulations of pipe flow at $R = 2000$, $R = 2800$, and $R = 4500$. $\sqrt{u_r^2 + u_\theta^2}$ is plotted in the reference frame moving at the neutral speed. White lines indicate front speeds from the model converted to physical units. At $R = 2000$ turbulence is localised with equal upstream and downstream front speeds. At $R = 4500$ turbulence expands with a strong downstream front and the long-time flow is fully turbulent. Note the upstream and downstream fronts have the same character (compare with the symmetric overshoot in Fig. 2d) and the spreading is symmetric in the neutral reference frame. At $R = 2800$ the downstream front moves at a speed between the weak and strong branches and exhibits some characteristics of both fronts as it fluctuates. This, as well as the intermittent laminar patches appearing within the turbulent flow are typical of turbulence as fully turbulent flow first arises.

Explaining the origin of the fully turbulent state is a decisive step towards connecting these regimes and paves the way for a bottom up approach to turbulence.

Acknowledgements

We thank A.P. Willis for sharing his hybrid spectral finite-difference code, Xiaoyun Tu for helping to set up and test the experiment. We acknowledge the Deutsche Forschungsgemeinschaft (Project No. FOR 1182), and the European Research Council under the European Union's Seventh Framework Programme (FP/2007-2013)/ERC Grant Agreement 306589 for financial support. Baofang Song acknowledges financial support from the Chinese State Scholarship Fund under grant number 2010629145. We acknowledge computing resources from GWDG (Gesellschaft für wissenschaftliche Datenverarbeitung Göttingen) and the Jülich Supercomputing Centre (grant HGU16) where the simulations were performed.

Author contributions

V.M., G.L. and B.H. designed and performed the experiments. V.M. analysed the experimental results. B.S. and M.A. designed and performed computer simulations of the Navier–Stokes equations, analysed the results and generated corresponding visualisations. D.B. performed the theoretical analysis. D.B., B.S., V.M., G.L., M.A and B.H. wrote the paper.

Correspondence

Supplementary information is available in the online version of the paper. Correspondence and requests for materials should be addressed to D.B. (email: D.Barkley@warwick.ac.uk) for theoretical aspect or B.H. (email: bhof@ist.ac.at) for experimental aspects.

Competing Interests

The authors declare that they have no competing financial interests.

1 Materials and methods

Speeds of laminar-turbulent fronts have been measured in detailed experiments and highly resolved computer simulations. In both cases long observation times were necessary to average out stochastic fluctuations that, although intrinsic to turbulence, may disguise the underlying transition scenario.

1.1 Pipe experiments

Experiments were carried out in a $D = 10\text{mm}$ ($\pm 0.01\text{mm}$) diameter pipe with a length of $1500D$. The 15m long pipe was assembled on a straight aluminium base and made of precision bore glass tubes with lengths between 1m and 1.2m . Customised connectors made from perspex allowed an accurate fit of the pipe segments. A specially made pipe inlet consisting of several meshes and a smooth convergence from a 100mm wide section to the 10mm pipe was used to avoid inlet disturbances and eddie formation (see Samanta *et al.*¹⁷ for details). In this way the water flow could be held laminar for R in excess of 8000.

The laminar flow was then left to develop its parabolic profile over a length of $200D$. At this downstream location, the flow could be perturbed by an impulsive jet of water injected (for 10ms) through a 1mm hole in the pipe wall. The perturbed flow was then left to grow into a turbulent patch over the next 250 pipe diameters and at this location (i.e. $450D$ from the inlet), a pressure sensor recorded the arrival of the upstream and downstream laminar turbulent interfaces. A second sensor was located a further $1000D$ downstream (i.e. $50D$ upstream of the pipe exit) again determining the arrival of the interfaces so that the average interface speed over the intermediate stretch of $1000D$ was measured. At each Reynolds number, the measurement of the interface velocity was repeated 10 times.

The flow was gravity driven from a reservoir at a fixed height above the pipe exit. Since during the course of a measurement the turbulent fraction in the pipe is increasing, the overall drag in the pipe also increases (turbulent flow has a higher skin friction than laminar flow). This unavoidably leads to a drop in the flow rate (and hence R) during a measurement. In order to minimise this effect, a large reservoir height was chosen; in this case $23m$ above the pipe exit. A precision valve positioned directly in front of the pipe inlet was used to adjust the flowrate and hence to select R . For the Reynolds number regime investigated here the total pressure drop across the pipe is much smaller than the $23m$ water head and most of the pressure drop occurs across the valve. The increase in drag caused by the expansion of turbulence is only a small fraction (smaller than 0.5% of the overall pressure drop) and hence even at the highest Reynolds numbers investigated flow rates were constant to within better than 0.5% throughout the measurement.

1.2 Duct experiments

Experiments were carried out in a square duct with width $h = 5mm$ and a length of $1200h$ ($6m$). The duct was made of 8 perspex sections precisely machined to an accuracy of $\pm 0.01mm$. They were assembled and mounted straight together on an aluminium frame. A well designed entrance section consisting of a honeycomb and a convergent section, with an area ratio of 25, allowed the flow to remain laminar up to, at least, $R = 5000$, where $R = u_{\text{bulk}}h/\nu$.

The flow was gravity driven from a reservoir at a fixed height and water was used as working fluid. Analogous to the pipe experiment a precision valve was positioned directly in front of the duct and was used to set the flowrate. The pressure drop across the valve was considerably larger than that across the pipe. The temperature of the water was controlled by means of an heat exchanger that the water had to pass before entering the pipe. Overall an accuracy in R of better than 0.5% was achieved for the investigated Reynolds number regime.

The flow was perturbed by injecting water through a $0.5mm$ hole drilled in one wall of the duct

120*h* downstream from the inlet. The duration of the perturbation was varied with R so that in dimensionless units it corresponded to $5h/U$. The evolution of the perturbation was then monitored at five locations where the pressure was recorded. The pressure sensors were positioned at 100*h*, 400*h*, 600*h*, 800*h* and 1000*h* downstream of the perturbation point. Sensors measured the pressure difference over 10*h* along the duct. The arrival times of both interfaces were detected at each location and the overall speeds were determined by a linear fit. For each R , we averaged the measurement over at least 50 realisations.

1.3 Numerical simulations

We consider the motion of incompressible fluid driven through a circular pipe with a fixed mass-flux. Normalising lengths with the diameter D and velocities with the bulk velocity U_{bulk} , the Navier-Stokes equations read

$$\frac{\partial \mathbf{u}}{\partial t} + \mathbf{u} \cdot \nabla \mathbf{u} = -\nabla p + \frac{1}{R} \Delta \mathbf{u}, \quad \nabla \cdot \mathbf{u} = 0$$

where \mathbf{u} is the velocity of the fluid and p the pressure. The Reynolds number is $R = U_{\text{bulk}}D/\nu$, where ν is the kinematic viscosity. These equations were solved in cylindrical coordinates (r, θ, z) using a code developed by Ashley P. Willis,³¹ employing a spectral-finite difference method with no-slip boundary conditions at the pipe wall $\mathbf{u}(1/2, \theta, z, t) = \mathbf{0}$ and periodicity in the axial direction. The pressure term was eliminated from the equations by using a Toroidal-Poloidal potential formulation of the velocity field, in which the velocity is represented by toroidal ψ and poloidal potentials ϕ , such that $\mathbf{u} = \nabla \times (\psi \hat{\mathbf{z}}) + \nabla \times \nabla \times (\phi \hat{\mathbf{z}})$.

After projecting the curl and double curl of the Navier-Stokes equations on the z -axis, a set of equations for the potentials ψ and ϕ is obtained. A difficulty, due to the coupled boundary conditions on the potentials, is solved with an influence-matrix method. In the radial direction spatial discretization is performed using finite difference method with a 9-point stencil. Assuming periodicity in azimuthal and axial directions, the unknowns, i.e., the potentials, are expanded in Fourier

modes,

$$A(r, \theta, z, t) = \sum_{k=-K}^K \sum_{m=-M}^M \hat{A}_{k,m}(r, t) e^{(i\alpha kz + im\theta)}$$

where αk and m give the wavenumbers of the modes in the axial and azimuthal directions respectively, $2\pi/\alpha$ fixes the pipe length L_z , and $\hat{A}_{k,m}$ is the complex Fourier coefficient of mode (k, m) . The time-dependent equations are integrated in time using a second-order predictor-corrector scheme with a dynamic timestep size, which is controlled using information from a Crank-Nicolson corrector step. The nonlinear term is evaluated using a pseudo-spectral technique with the de-aliasing $\frac{3}{2}$ -rule. With expansion (1.3), the resulting linear differential equations for the potentials ψ and ϕ decouple for each (k, m) mode. These are solved using an LU decomposition of the resulting banded matrices. See³¹ for more the details of the formulation and solution.

Initial conditions were prepared at $R = 2000$ in $133D$ and $180D$ pipes for simulations at $R > 2000$. At low $R \gtrsim 2000$ puff-splitting is extremely unlikely⁷ and puffs remain approximately constant in length (about $20D$) as they travel downstream along the pipe. Hence simulations at $R = 1910, 1920, 2000$ were carried out in a shorter $24\pi \approx 75D$ pipe, with initial conditions prepared at $R = 1950$. In Table S1 the length of the pipes and numerical resolutions used at each Reynolds number are listed.

The fronts were detected by setting an appropriate cut-off. In this paper, the local intensity was computed as

$$\int \int (u_r^2 + u_\theta^2) r dr d\theta,$$

and a cut-off of 5×10^{-4} was chosen for all the simulations to determine the position of laminar-turbulent fronts. We tested different cut-off values and found that the front speed was insensitive to them.

The expansion speed of the downstream front was found to accelerate substantially during the initial stages of the simulation. In order to obtain the asymptotic value of the speed, we determined the length of the turbulent region L_0 beyond which the speed statistics become length-independent.

R	$L_z(D)$	N	K	M	R	L_z	N	K	M
1910	24π	48	640	32	3000	180	72	2560	48
1920	24π	48	640	32	3200	180	72	2560	54
2000	24π	48	768	40	3500	180	72	2560	54
2200	133	48	768	40	3750	133	72	2048	54
2300	133	64	1536	40	4000	133	72	2048	54
2400	133	64	2048	48	4500	180	80	3072	64
2800	180	72	2560	48	5000	180	80	3072	64
2600	133	64	2048	48	5500	180	96	3840	80

Table S1: The domain size and resolution for the simulation at all the Reynolds numbers we considered. Note that in physical space there are $3K$ and $3M$ grid points in axial and azimuthal directions.

We found that for $R < 4000$, $L_0 > 60D$ was sufficient, whereas for $R \geq 4000$ $L_0 > 100D$ was required. This is the reason why very long pipes as reported in Table S1 were used. At each R the speed was determined by computing $(z_{\text{end}} - z_0)/(t_{\text{end}} - t_0)$ for each run and then averaging over a total of 20 runs. The initial time t_0 corresponds here to the time at which the turbulent region has reached the length L_0 .

2 Theory

2.1 Model details

The model is a two-component system of advection-reaction-diffusion equations

$$\frac{\partial q}{\partial t} + (u - \zeta) \frac{\partial q}{\partial x} = f(q, u) + D \frac{\partial^2 q}{\partial x^2}, \quad \frac{\partial u}{\partial t} + u \frac{\partial u}{\partial x} = \epsilon g(q, u) \quad (\text{S3})$$

where q represents the level of turbulent fluctuations and u the axial velocity on the centreline. The nonlinear reaction functions f and g are given by

$$f(q, u) = q(r + u - 2 - (r + 0.1)(q - 1)^2), \quad g(q, u) = 2 - u + 2q(1 - u)$$

where the parameter r corresponds to a suitably scaled Reynolds number.

The model and the role of the fitting parameters (D , ζ and ϵ) are most easily understood by first considering the equations in the absence of spatial derivatives. In this case the model reduces to the ordinary differential equations (ODEs)

$$\dot{q} = f(q, u), \quad \dot{u} = \epsilon g(q, u)$$

These ODEs are the core of the model as they describe the interaction between the turbulent fluctuations q and axial velocity u locally in space. The functional forms are designed to qualitatively capture the well-established physics of this interaction^{2,3} with minimal nonlinearities. (In a previous approach,²² the variable u corresponded to the axial velocity of pipe flow in the frame of reference moving at the bulk velocity U_{bulk} , here u corresponds to velocity in the lab frame so that $u = 2$ for laminar flow.)

The nullclines for the ODEs are given by $f(q, u) = 0$ and $g(q, u) = 0$. For all parameter values of the ODEs these nullclines intersect at the fixed point ($u = 2, q = 0$) corresponding to laminar, Hagen–Poiseuille flow. By design ϵ sets ratio of the time scale of u relative to q . (Previously,²² parameters ϵ_1 and ϵ_2 appeared in the model. Here we have a simplified the model to a single time-scale ratio ϵ . In terms of ϵ , the previous parameters would be $\epsilon_1 = \epsilon$ and $\epsilon_2 = 2\epsilon$.)

Now consider the full model equations. In addition to the local terms given by f and g , the model has first and second spatial derivatives. The first derivative terms account for nonlinear advection in the streamwise direction. For the u equation we use the advective nonlinearity following directly from the Navier–Stokes equations. For the turbulent field q , the parameter ζ accounts for a diminished advection of q in comparison with the centreline velocity u . The streamwise velocity is

maximal on the centreline and the turbulent field is not advected at this speed. We have simulated turbulent flow in short pipes ($L = 12D$) and have verified that turbulent structures are advected considerably more slowly than the centreline velocity. This effect involves complex processes in the pipe cross-section. We include in the model the simplest term that can account for diminished advection. (Previously,²² the model contained only linear advection, the fixed difference in the advection of the q and u fields was expressed by an additional first-derivative term on the right-hand-side of the u -equation. This effectively corresponded to $\zeta = 1$ in the current model.) We return to the importance of the parameter ζ after we derive expressions for front speeds in the model.

The diffusive term in equation (S3) accounts for the processes by which a region of turbulence flow couples to and thereby excites adjacent laminar flow. The physical processes involved are complex and not fully understood.^{3,7,16,20,32,33} The second-derivative is the most natural choice for modelling such a coupling. The coupling strength, or diffusion coefficient, D is the final model parameter.

2.2 Asymptotic analysis

The asymptotic analysis follows very closely that of.²⁹ Let the three roots of f be noted q^0, q^\pm . The laminar branch is $q^0 = 0$ for all u and r , while the upper and lower branches q^\pm are functions of u and r . The laminar q^0 and upper q^+ branches are stable. For small ϵ the dynamics of the system separates into slow regions and fast front regions. In the slow regions the system is slaved to one of the stable branches (slow manifolds) and u evolves on a slow scale, e.g. along the upper branch q^+

$$q = q^+(u), \quad \frac{\partial u}{\partial t'} + u \frac{\partial u}{\partial x'} = g(q^+(u), u)$$

where $x' = \epsilon x$ and $t' = \epsilon t$ are slow scales.

In the fast regions, fronts are formed as the system transitions between the stable branches, from

q^0 to q^+ as x increases for an upstream front while q^+ to q^0 for a downstream front. Let c denote the speed of the front and go into a frame of reference moving at speed c . Locate the now stationary front at $x = 0$ and work in an inner (stretched) variable. At leading order in ϵ the equations in the stretched coordinate become

$$q'' + sq' + f(q, u) = 0, \quad (\text{S4})$$

$$u' = 0 \quad (\text{S5})$$

where

$$s \equiv \frac{c - (u_f - \zeta)}{\sqrt{D}}$$

From Eq. (S5), at leading order u is constant across a front. Call this constant value u_f . Equation (S4) must be solved subject to boundary conditions. For a downstream front these are

$$q(-\infty) = q^+(u_f), \quad q(+\infty) = q^0 \quad (\text{S6})$$

For an upstream front the boundary conditions are reversed, but this can be accounted for by a change of sign of s in Eq. (S4).

In summary, the speed of a front at given value of $u = u_f$ is found by solving

$$q'' + sq' + f(q, u_f) = 0 \quad (\text{S7})$$

subject to boundary conditions (S6). This will give a value of s , which will depend on u_f and r . Denote it $s(u_f, r)$. From this the front speed is

$$c = u_f - \zeta \pm \sqrt{D} s(u_f, r) \quad (\text{S8})$$

with $+$ for a downstream front and $-$ for an upstream front. For the strong downstream front and all upstream fronts, $u_f = 2$. Hence their speeds are

$$c = 2 - \zeta \pm \sqrt{D} s(2, r) \quad (\text{S9})$$

For the weak downstream front $u_f = u_{ss}$ where u_{ss} is the upper branch steady state. Hence

$$c = u_{ss} - \zeta + \sqrt{D} s(u_{ss}, r) \quad (\text{S10})$$

Figure S1 shows model front speeds as a function of model Reynolds number. Figure S1b is the same as Fig. 2g in the main paper, except over a smaller range of r . Speeds are from Eqs. (S9) and (S10).

Note that the neutral speed in the model is $2 - \zeta$. This follows immediately from Eq. (S9) where one can see that the upstream speed (minus sign) and strong downstream speed (plus sign) are symmetric with respect to $2 - \zeta$. This is the advection speed of turbulence in the absence of front dynamics due to transitions between laminar and turbulent flow. Without the parameter ζ , the neutral speed would be the maximum centreline velocity. This is neither consistent with the observed neutral speed, nor is it reasonable that turbulent structures would be advected at the *maximum speed found in the flow*.

Figure S1a shows front speeds without the inclusion of advection terms (first derivatives in x) in the model equations. Without these terms the front speeds become

$$c = \pm\sqrt{D} s(2, r)$$

for the strong downstream front and all upstream fronts, and

$$c = \sqrt{D} s(u_{ss}, r)$$

for the weak downstream front. The transition to expanding turbulence is discontinuous. Including linear advection (as was done previously²²) will result in an overall shift in all front speeds, and can affect the asymptotic stability of branches (technical details on stability for the asymptotic branches will be presented elsewhere) but will not change the discontinuous nature of the transition.

This highlights the role of nonlinear advection in the bifurcation scenario: without the physical affect of nonlinear advection the weak front branch has a distinct critical point and the transition to expanding turbulence is first-order (discontinuous).

Note that in Figs. 2a, 2b, and 2c, of the main paper, solutions $q(x)$ are obtained directly from the full model equations at $\epsilon = 0.01$, which is sufficiently small that these solutions are visually close

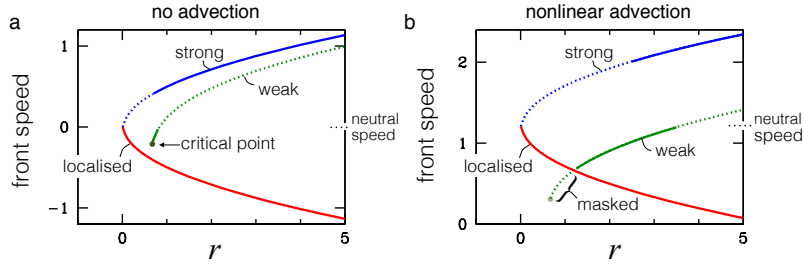


Figure S1: **Speed of model fronts in the asymptotic limit of sharp fronts.** Speeds as a function of model Reynolds number r both **a** without and **b** with advection. While strong downstream fronts cannot exist and have no physical meaning below the formation of the upper branch fixed point, the expression for strong front speeds (S9) still gives the speed such a strong downstream front would have and these speeds are shown as dashed. The effect of nonlinear advection in **b** is to mask the nominal critical point for the onset of fully turbulent flow. The neutral speed is naturally displaced from the bulk speed $U_{\text{bulk}} = 1$.

approximations to the $\epsilon \rightarrow 0$ limit. Figures 2d, 2e, 2f, show the nullclines for exactly the cases shown in Figs. 2a, 2b, and 2c; however, the phase portraits are sketches. This both facilitates the colouring of the front branches and also, even at $\epsilon = 0.01$, the jumps between the branches of q are not seen as completely vertical in the phase plane.

It is well established that exact coherent structures in pipe flow lie along upper and lower branches. Most known exact solutions are spatially extended, in the form of travelling waves,^{25–27,34} but recently spatially localised states were also found.^{35,36} The model captures these states in a minimal way. The fixed points (one stable and one unstable) arising as the model transitions to bistability can be viewed as upper and lower branches of spatially extended travelling-wave solutions. The cubic nonlinearity in f is that minimally required for this separation into upper and lower branch states. The model also has localised states (puffs) and importantly unstable small-amplitude localised solutions (not discussed in this paper, but see Refs.^{22,28,29}) corresponding to edge states, both in the puff regime and in the fully turbulent regime.

Finally, we comment on what takes place at the critical point. As with all material in this section, the discussion follows closely Refs.^{28,29} Figure S2 illustrates solutions to the boundary value problem (S7) in the case of a downstream front. For a fixed value of r , the eigenvalue s and solution q depend on u_f , the value of u at the front. Note in particular that the boundary conditions (S6) depend on u_f .

Downstream fronts are heteroclinic connections from q^+ to q^0 , where “time” in the phase plane corresponds to space x . The phase plane is two-dimensional, coordinates q and q' , because Eq. (S7) is a second order differential equation. As illustrated in Fig. S2c, for generic u_f , both q^+ and q^0 are hyperbolic fixed point (saddles) in the phase plane and hence a heteroclinic connection exists only for a unique value of s . This determines s as a function of u_f , as shown by the bold curve in Fig. S2a. However, when u_f takes the value such that $q^+ = q^-$, i.e. at the nose of the q nullcline, then the upper fixed point is no longer hyperbolic and there exist infinitely many heteroclinic connections from q^+ to q^0 , and hence infinitely many possible values of s . These appear as the thin line in Fig. S2a.

Now, as the parameter r is varied (as in Fig. 2 of the main paper), the nullclines vary. The critical point is where upper branch steady state occurs at the limit point of the q nullcline, that is the upper fixed point is at $q^+ = q^-$. For r smaller than this value, the downstream front can take any of an infinite range of values because the downstream front can occur at a value of $u_f = u_c$. For a puff, this infinite range of possible values is the mechanism that allows the speed of the downstream front to select the same value as for the upstream front. As a result puffs remain localised while traveling along the pipe. However, for r larger than the critical value the upper branch fixed point no longer permits downstream fronts to occur at $u_f = u_c$, as seen in (as in Fig. 2e of the main paper). This restricts the possible values of s , and hence possible speeds of the downstream front, to the bold portion of the branch illustrated in Fig. S2a. Hence, as r passes through the critical point there is an abrupt change in the allowed values of the downstream front speeds, from an infinite to a finite range. Without nonlinear advection, the abrupt change is manifested as a discontinuous change in the speed of the downstream front. With nonlinear advection, there is still an discontinuous

change to the allowed values of s , but the speeds are smaller than those of the upstream front, so the discontinuity in allowed solutions is masked.

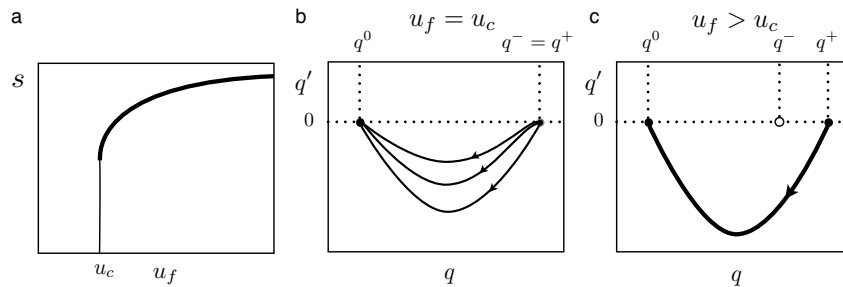


Figure S2: **Front speeds at critical point.** Sketch illustrating solutions to the boundary value problem (S7) for a downstream front near the critical point. **a**, eigenvalue s as a function of u_f . u_c is the value of u_f such that $q^- = q^+$. For this value there are infinitely many possible eigenvalues s indicated by a thin line. **b,c** phase planes (q, q') showing solutions for the second order differential equation (S7). Downstream fronts are heteroclinic connections from the upper fixed point q^+ to the lower fixed point q^0 . When $u_f = u_c$ and hence $q^- = q^+$, the upper fix point is not hyperbolic and there are infinitely many connections, each corresponding to a value of s . When $u > u_c$, q^+ is hyperbolic and there is a unique connection and hence a unique solution s .

2.3 Collapsing pipe and duct data

In order to collapse data from pipe and duct flow onto a single plot, it is necessary to determine specific Reynolds numbers and speeds from measured data (see figure S3) which will then be used to align the data from the two flows. We stress that while the procedure is informed from the model analysis, it requires only measured data and the same procedure could be applied to data from other shear flows.

Figures S3 **a** and **c** show data from pipe and duct flow, respectively, plotted with the upstream speeds additionally reflected about the neutral speed, here labelled C_0 . The value of C_0 is deter-

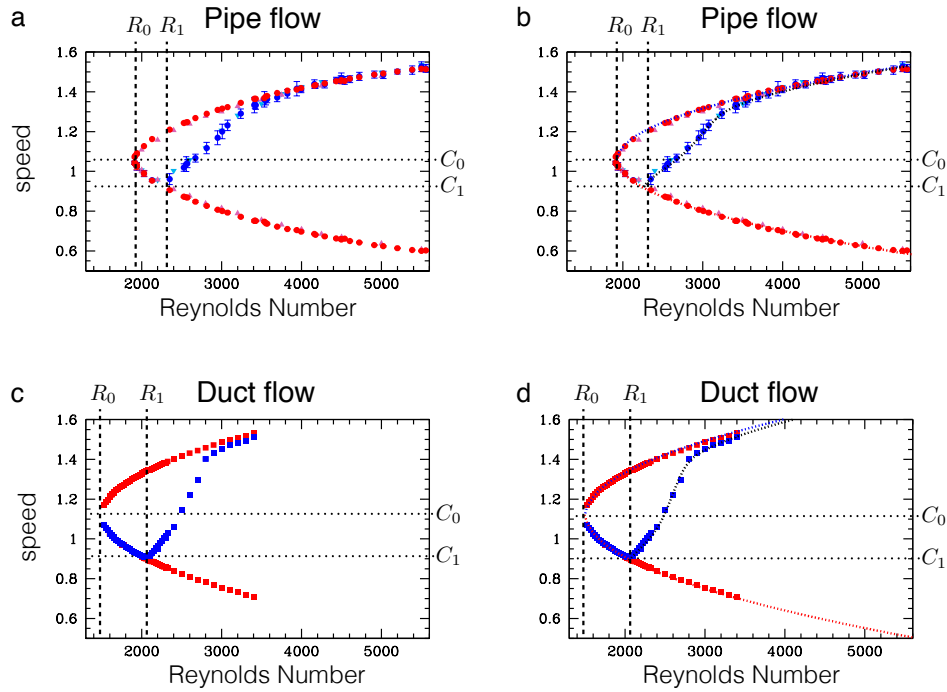


Figure S3: **Determination of corresponding Reynolds numbers and speeds for pipe and duct flow.** Speeds from pipe and duct flow are plotted, as in Fig. 1c of the main paper, but additionally with the upstream front speeds reflected about the neutral speed C_0 . Left column shows only experimental and simulation data while the right column includes also model fits to the data. The determined values for R_0 , R_1 , C_0 , C_1 , are: $R_0 = 1920$, $C_0 = 1.06$, $R_1 = 2250$, and $C_1 = 0.92$ for pipe flow, and $R_0 = 1490$, $C_0 = 1.12$, $R_1 = 2030$, and $C_1 = 0.90$ for duct flow.

mined to be that for which reflected upstream data coincides with the downstream data at sufficiently large Reynolds number. Figures S3 **b** and **d** show the same data, but with model speeds (determined subsequently) also plotted to additionally guide the eye. In the case of pipe flow it is possible to determine C_0 to better than 2% accuracy by the procedure. For duct flow, our estimation is that the downstream front speed has not quite reached the reflected upstream speed at the highest Reynolds number accessible to present experiments. Nevertheless, C_0 is still quite well determined by this procedure. From the same plots, the value of the Reynolds number R_0 at which the upstream front obtains the neutral speed C_0 , is easily determined.

Then, from the data, we determine the Reynolds number R_1 where the downstream weak front first deviates from the downstream front. Again, this can in principle be determined solely from the data, although using model fits to the weak branch can give further confidence in the determined values. C_1 is the value of the front speed at R_1 .

Once the values (R_0, C_0) and (R_1, C_1) have been found for each flow, the data can be collapsed by plotting each data set to align the two points (R_0, C_0) and (R_1, C_1) , as seen in figure S4. This is equivalent to simply choosing the origin and scaling for the axes for the two flows. The upstream and strong downstream fronts each collapse, while the weak-front branch does not.

2.4 Determining model parameters

There are three model parameters, namely D , ζ , and ϵ , to be determined to quantitatively relate the model speeds to the measured data for each flow.

The generic model cannot be expected to predict the flow specific values R_0 , R_1 , C_0 , and C_1 , and moreover there is nothing universal about these values. Instead, given these flow-specific values, the model is expected to capture the form of the various branches seen in the collapsed data of Fig. S4. For fitting model parameters it is useful to plot the collapsed data in terms of reduced

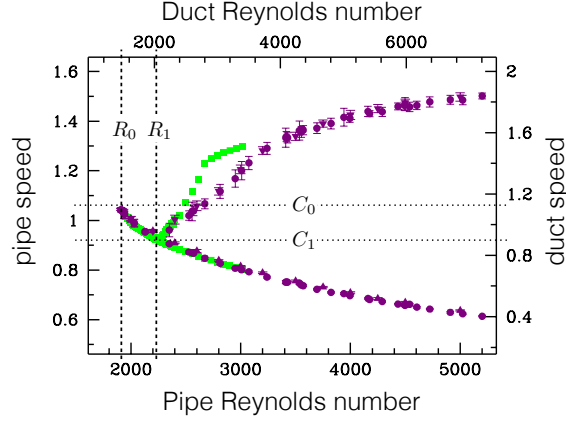


Figure S4: **Collapse of pipe and duct data.** Pipe and duct flow are plotted together using different axes. The data are plotted such as to align the two points (R_0, C_0) and (R_1, C_1) for each data set, e.g. $(R_1, C_1) = (2250, 0.92)$ for pipe flow is aligned with $(R_1, C_1) = (2030, 0.90)$ for duct flow, bringing into alignment the onset of weak front.

Reynolds number and reduced speed

$$\frac{R - R_0}{R_1 - R_0}, \quad \frac{1}{2} \frac{C - C_0}{C_0 - C_1} \quad (\text{S11})$$

which amounts only to a relabelling of the axes in Fig. S4 to shift the neutral speed to zero and scale the onset of the weak front to the point $(1, -1/2)$. As will appear momentarily, the reason for including $1/2$ in the reduced speed is that model speeds are typically about half those of the reduced speeds for experimental data.

We first consider the value of the parameter D . We select D so as to fix a simple relationship between model and measured quantities for both flows. Specifically, in Fig. S5a we plot the collapsed pipe and duct data together with the asymptotic results from the model for different values of D . The model results are plotted directly in terms of model Reynolds number r and model speed $c - c_0$ (the model speed c shifted by the model neutral speed c_0). For $D = 0.13$ the upstream front and strong branches match the collapsed experimental data extremely well. Note, the strong and weak asymptotic curves in Fig. S5a are independent of the other two model parameters, ϵ and ζ .

The result is that using only one parameter, D , and fixing its value to 0.13, the model does not only fit very well the upstream and strong downstream front speeds for both flows, but also a simple relationship between model and experimental data is fixed, namely

$$r = \frac{R - R_0}{R_1 - R_0}, \quad c - c_0 = \frac{1}{2} \frac{C - C_0}{C_0 - C_1} \quad (\text{S12})$$

Given the flow specific values R_0 , R_1 , C_0 , and C_1 , Eqs. (S12) can be inverted to obtain Reynolds number R and speed C from the model values r and c . This is how model results are mapped to Reynolds number and speed in Fig. 3 of the main paper.

The remaining two model parameters dictate the behaviour of the downstream fronts as they transition from weakly expanding to strongly expanding. Here pipe and duct flow differ and so necessarily the values of the fitting parameters will be different for the two flows. See Fig. S5b.

The value of ϵ dictates how quickly the system jumps from the weak to the strong branch. Large values give smoother transitions while smaller values give more abrupt transitions. The value of ζ dictates how long the system follows the weak branch before transitioning to the strong branch. Larger values, as for pipe flow, result in a delay in transition, while smaller values of ζ , as for the fit to duct flow, result in more immediate transition. We did not apply a formal procedure for determining ζ and ϵ for each of the flows. Rather they were determined simply by eye. In both cases it is quite easy to adjust ζ and ϵ so that the transition from weak to strong front follows the measured data.

3 Control

The model suggests that the fully turbulent state can be destabilized by removing the upper turbulent fixed point as depicted in Fig. S6a. In the model this is achieved by forcing the variable u corresponding to the state of shear profile. The reduction of u by forcing corresponds to a blunting of the shear profile.

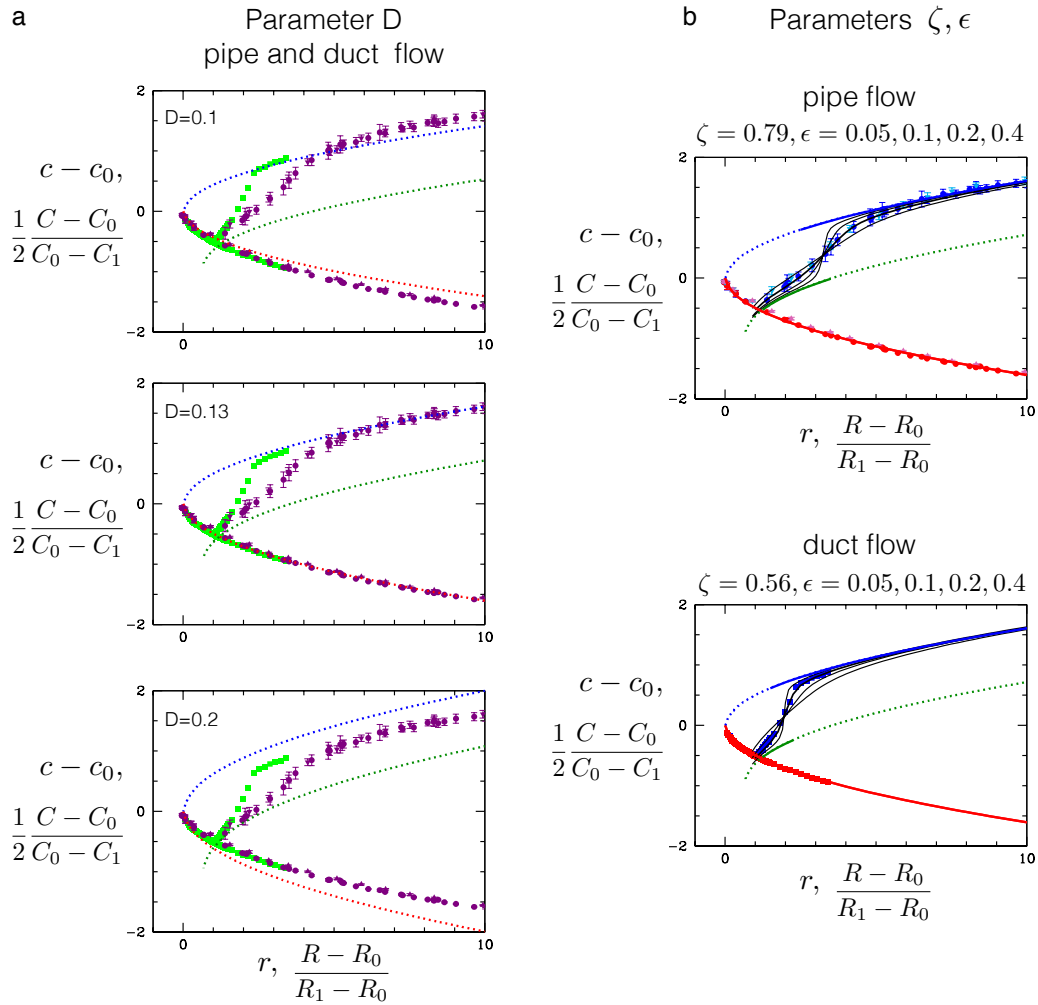


Figure S5: **Determination of model parameters for pipe and duct flow.** **a**, Determination of D . Points are collapsed data from pipe and duct flow (as in Fig. S4) here plotted in terms of reduced Reynolds number and reduced speed. Dotted curves are asymptotic speed curves (as in Fig. S1) plotted in term of model Reynolds number r and speed $c - c_0$. For $D = 0.13$ there is very good agreement between data and model. This choice fixes the asymptotic branches (dashed lines). **b**, Determination of ζ and ϵ . Pipe and duct flow are necessarily considered separately. In each case, downstream branches are shown for four values of ϵ . Smaller values give more abrupt transition between weak and strong branches.

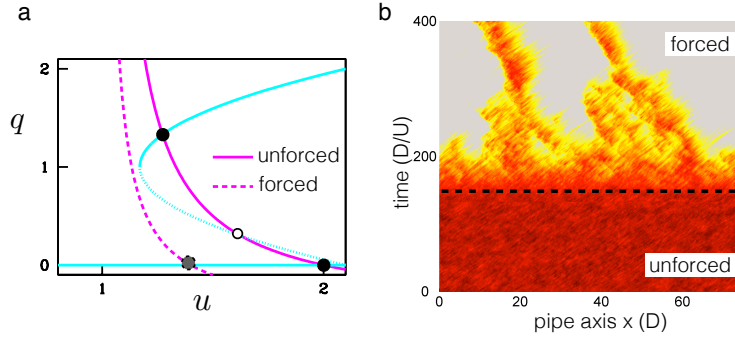


Figure S6: **Illustration of control based on removing turbulent fixed point.** **a**, control concept illustrated in the model phase plane. Without forcing (i.e. without control), there is an upper branch fixed point (upper intersection of nullclines) corresponding to fully turbulent flow. Applying an additive forcing term to the u -equation corresponds to forcing the shear profile and blunting its shape. This can remove the turbulent fixed point thus eliminating fully turbulent flow. **b**, Proof of concept in a direct numerical simulation of pipe flow at $R = 5000$. Without forcing the flow is fully turbulent. A global body force is applied and blunts the velocity profile to a more plug-like form. Subsequently, only localised turbulent patches remain, reminiscent of those at much lower R .

To demonstrate that the fully turbulent state can indeed be destabilized by removing the turbulent fixed point, as suggested by the model, we have performed a direct numerical simulation of pipe flow at $R = 5000$. Initially the forcing is not applied and the flow is fully turbulent. Starting at time 175 a global body force is gradually switched on (fully applied by time 200) which blunts the velocity profile to a more plug-like form (the same forcing is used as in Hof *et al.*¹⁸). As can be seen, turbulent intensity subsequently decreases and eventually the fully turbulent flow destabilizes and degenerates into localised turbulent patches, just as the natural ones (puffs) at lower Reynolds number (below ~ 2300) in the absence of any additional force. Further details will be presented elsewhere.

- ¹ Reynolds, O. An experimental investigation of the circumstances which determine whether the motion of water shall be direct or sinuous, and of the law of resistance in parallel channels. *Phil. Trans. R. Soc. Lond. A* **174**, 935—982 (1883).
- ² Coles, D. Interfaces and intermittency in turbulent shear flow. *Mécanique de la Turbulence* 229 (1962).
- ³ Wygnanski, I. J. & Champagne, F. H. On transition in a pipe. Part 1. The origin of puffs and slugs and the flow in a turbulent slug. *J. Fluid Mech.* **59**, 281–335 (1973).
- ⁴ Sreenivasan, K. R. & Ramshankar, R. Transition intermittency in open flows, and intermittency routes to chaos. *Physica D* **23**, 246–258 (1986).
- ⁵ Nishi, M., Ünsal, B., Durst, F. & Biswas, G. Laminar-to-turbulent transition of pipe flows through puffs and slugs. *J. Fluid Mech.* **614**, 425–446 (2008).
- ⁶ Mullin, T. Experimental studies of transition to turbulence in a pipe. *Annual Review of Fluid Mechanics* **43**, 1–24 (2011).
- ⁷ Avila, K. *et al.* The onset of turbulence in pipe flow. *Science* **333**, 192–196 (2011).
- ⁸ Pope, S. B. *Turbulent flows* (Cambridge university press, 2000).
- ⁹ Schlichting, H. & Gersten, K. *Boundary-layer theory* (Springer, 2000), 8th edn.
- ¹⁰ Emmons, H. W. The laminar-turbulent transition in a boundary layer. *J. Aero. Sci.* **18**, 490 (1951).
- ¹¹ Coles, D. Transition in circular Couette flow. *J. Fluid Mech.* **21**, 385–425 (1965).
- ¹² Lundbladh, A. & Johansson, A. V. Direct simulation of turbulent spots in plane Couette flow. *J. Fluid Mech.* **229**, 499–516 (1991).
- ¹³ Tillmark, N. & Alfredsson, P. H. Experiments on transition in plane Couette flow. *J. Fluid Mech.* **235**, 89–102 (1992).

- ¹⁴ Cros, A. & Le Gal, P. Spatiotemporal intermittency in the torsional Couette flow between a rotating and a stationary disk. *Physics of Fluids (1994-present)* **14**, 3755–3765 (2002).
- ¹⁵ Lemoult, G., Aider, J.-L. & Wesfreid, J. E. Turbulent spots in a channel: large-scale flow and self-sustainability. *Journal of Fluid Mechanics* **731**, R1 (2013).
- ¹⁶ Moxey, D. & Barkley, D. Distinct large-scale turbulent-laminar states in transitional pipe flow. *Proc. Natl. Acad. Sci. USA* **107**, 8091 (2010).
- ¹⁷ Samanta, D., de Lozar, A. & Hof, B. Experimental investigation of laminar turbulent intermittency in pipe flow. *J. Fluid Mech.* **681**, 193–204 (2011).
- ¹⁸ Hof, B., De Lozar, A., Avila, M., Tu, X. & Schneider, T. Eliminating turbulence in spatially intermittent flows. *Science* **327**, 1491 (2010).
- ¹⁹ Lindgren, E. R. The transition process and other phenomena in viscous flow. *Arkiv Fysik* **12** (1957).
- ²⁰ Duguet, Y., Willis, A. P. & Kerswell, R. R. Slug genesis in cylindrical pipe flow. *J. Fluid Mech.* **663**, 180–208 (2010).
- ²¹ Sipos, M. & Goldenfeld, N. Directed percolation describes lifetime and growth of turbulent puffs and slugs. *Phys. Rev. E* **84**, 035304 (2011).
- ²² Barkley, D. Simplifying the complexity of pipe flow. *Phys. Rev. E* **84**, 016309 (2011).
- ²³ Barkley, D. Modeling the transition to turbulence in shear flows. *Journal of Physics: Conference Series* **318**, 032001 (2011).
- ²⁴ Barkley, D. Pipe flow as an excitable medium. *Rev. Cub. Fis.* **29**, 1E27 (2012).
- ²⁵ Eckhardt, B., Schneider, T. M., Hof, B. & Westerweel, J. Turbulence transition in pipe flow. *Ann. Rev. Fluid Mech.* **39**, 447–468 (2007).
- ²⁶ Gibson, J., Halcrow, J. & Cvitanović, P. Three-dimensional finite-amplitude solutions in plane Couette flow: bifurcation from infinity. *J. Fluid Mech.* **611**, 107–130 (2008).

- ²⁷ Kawahara, G., Uhlmann, M. & van Veen, L. The significance of simple invariant solutions in turbulent flows. *Ann. Rev. Fluid Mech.* **44**, 203–225 (2011).
- ²⁸ Rinzel, J. & Terman, D. Propagation phenomena in a bistable reaction-diffusion system. *SIAM J. Appl. Math.* **42**, 1111–1137 (1982).
- ²⁹ Tyson, J. & Keener, J. Singular perturbation-theory of traveling waves in excitable media. *Physica D* **32**, 327–361 (1988).
- ³⁰ Avila, M. & Hof, B. Nature of laminar-turbulence intermittency in shear flows. *Phys. Rev. E* **87**, 063012 (2013).
- ³¹ Willis, A. P. & Kerswell, R. R. Turbulent dynamics of pipe flow captured in a reduced model: puff relaminarization and localized ‘edge’ states. *J. Fluid Mech.* **619**, 213–233 (2009).
- ³² Wygnanski, I., Sokolov, M. & Friedman, D. On transition in a pipe. Part 2. The equilibrium puff. *J. Fluid Mech.* **69**, 283–304 (1975).
- ³³ Holzner, M., Song, B., Avila, M. & Hof, B. Lagrangian approach to laminar–turbulent interfaces in transitional pipe flow. *J. Fluid Mech.* **723**, 140–162 (2013).
- ³⁴ Kerswell, R. R. Recent progress in understanding the transition to turbulence in a pipe. *Nonlinearity* **18**, R17 (2005).
- ³⁵ Avila, M., Mellibovsky, F., Roland, N. & Hof, B. Streamwise-localized solutions at the onset of turbulence in pipe flow. *Phys. Rev. Lett.* **110**, 224502 (2013).
- ³⁶ Chantry, M., Willis, A. P. & Kerswell, R. R. Genesis of streamwise-localized solutions from globally periodic traveling waves in pipe flow. *Phys. Rev. Lett.* **112**, 164501 (2014).